


# Facile hydrothermal synthesis and characterization of cesium-doped $\text{PbI}_2$ nanostructures for optoelectronic, radiation detection and photocatalytic applications

Mohd Shkir  · S. AlFaify · I. S. Yahia ·  
Mohamed S. Hamdy · V. Ganesh · H. Algarni

Received: 19 May 2017 / Accepted: 7 September 2017 / Published online: 26 September 2017  
© Springer Science+Business Media B.V. 2017

**Abstract** Low-temperature hydrothermal-assisted synthesis of pure and cesium (Cs) (1, 3, 5, 7 and 10 wt%) doped lead iodide ( $\text{PbI}_2$ ) nanorods and nanosheets have been achieved successfully for the first time. The structural and vibrational studies confirm the formation of a 2H-polytypic  $\text{PbI}_2$  predominantly. Scanning electron microscope analysis confirms the formation of well-aligned nanorods of average size  $\sim 100$  nm at low concentration and nanosheets of average thicknesses in the range of  $\sim 20$ – $40$  nm at higher concentrations of Cs doping. The presence of Cs doping was confirmed by energy dispersive X-ray study. Ultra-violet-visible absorbance spectra were recorded, and energy gap was calculated in the range of 3.33 to 3.45 eV for pure and Cs-doped  $\text{PbI}_2$  nanostructures which is higher than the bulk value (i.e.,  $\sim 2.27$  eV) due to quantum confinement effect. Dielectric constant, loss, and AC conductivity studies have been done. Enhancement in Gamma linear absorption coefficient due to Cs doping confirms the suitability of prepared nanostructures for radiation

detection applications. Furthermore, the photocatalytic performance of the synthesized nanostructures was evaluated in the decolorization of methyl green (MG) and methyl orange (MO) under the illumination of visible light ( $\lambda > 420$  nm). The observed photocatalytic activity for 5 and 7 wt% Cs-doped  $\text{PbI}_2$  was observed to be more than pure  $\text{PbI}_2$  and also  $> 10$  times higher than the commercially available photocatalysts. The results suggest that the prepared nanostructures are highly applicable in optoelectronic, radiation detection and many other applications.

**Keywords** Lead iodide · FT-Raman spectroscopy · SEM · Optical properties · Dielectric properties · Radiation studies · Semiconductor nanomaterials

## Introduction

Lead iodide ( $\text{PbI}_2$ ) is a wide band gap semiconductor material with layered structure which consists of a repeating unit of a hexagonally closed-packed layer of lead ions sandwiched between two layers of iodide ions. It comprises various key applications such as in the development of active matrix flat panel imagers (AMFPIs) and functions as detectors for X-ray digital radiography using direct conversion technique, mammography energy range detection, room temperature X-ray imaging, and nuclear particle detectors (Bennett et al. 2003; Ponpon 2005; Roth and Willig 1971; Street et al. 2002; Street et al. 1999). The other important applications of  $\text{PbI}_2$  are as radiation detector,

---

M. Shkir (✉) · S. AlFaify (✉) · I. S. Yahia · V. Ganesh ·  
H. Algarni  
Advanced Functional Materials and Optoelectronic Laboratory  
(AFMOL), Department of Physics, College of Science, King  
Khalid University, P.O. Box 9004, Abha 61413, Saudi Arabia  
e-mail: shkirphysics@gmail.com  
e-mail: shkirphysics@kku.edu.sa  
e-mail: sasaalfaify@hotmail.com

M. S. Hamdy  
Department of Chemistry, College of Science, King Khalid  
University, P.O. Box 9004, Abha 61413, Saudi Arabia

photoconductors, photo-detectors, photovoltaic, co-precipitation sensors, biological labeling and diagnostic, and light-emitting diodes including photo-electro-co-precipitation and in the fabrication of Perovskite solar cells, etc. (Antonuk et al. 2000; Bennett et al. 2003; Condeles and Mulato 2015b; George et al. 1994; Ponpon 2005; Shkir et al. 2012b; Tubbs and Forty 1964; Yu et al. 2015; Zentai et al. 2005). It is well known in the literature that the materials with well-organized nanostructure are one of the amazing fields of research and development and demandable for advanced technologies due to their extensive exploitation in the vicinity of optoelectronic devices (Ahn et al. 2015; Arico et al. 2005; Baxter and Aydil 2005; Empedocles et al. 2005; Goldberg et al. 2007; Liang et al. 2014; Scher et al. 2005; Warren and Liang 1993; Xu et al. 2012; Zhao et al. 2016). Nanostructured (nanocrystals, nanorods, nanotubes, nanowires, nanobelts, nanoribbons, nanosheets) semiconductor materials give outstanding quantum chattels. Due to robust applications of  $\text{PbI}_2$  in optoelectronic and room temperature radiation detection devices, the idyllic alternative is to nanostructure it. Quite a number of reports are available on  $\text{PbI}_2$  such as on its synthesis and nanostructurization by inverse microemulsion method, hydrothermal rout, reverse micelle solution technique, chemical route, microwave technique, etc. (Barnakov et al. 2001; Dag and Lifshitz 1996; Lifshitz et al. 1994; Ma et al. 2005; Sengupta et al. 2000; Shkir et al. 2016b; Tang et al. 1995; Zhu et al. 2010; ZHU et al. 2007a); the fabrication of pure and doped thin films (Albrecht and Green 1977; Bhavsar and Saraf 2003; Condeles et al. 2006; Condeles and Mulato 2015a; Condeles and Mulato 2016; Condeles et al. 2007; Dmitriev et al. 2009; Ghosh et al. 2008; Mousa et al. 2012; Shkir et al. 2012b; Zentai et al. 2005; Zhu et al. 2012); and the growth of pure and doped single crystals (Bhavsar 2011; Matuchova et al. 2006; Novosad and Novosad 2013; Ponpon and Amann 2004; Sandroff et al. 1986; Tonn et al. 2011; Tonn et al. 2015; Zhang et al. 2015) and have extensively studied various key characteristics and demonstrated a visible alteration in its properties when it is in nano-films/nanoparticles/nanostructures form. In these reports, the properties such as structural, optical, and electronic are found to be varied. Freshly, the synthesis of  $\text{Gd}^{3+}$ -doped  $\text{PbI}_2$  nanosheets has been prepared by hydrothermal and microwave route by our group (Shkir et al. 2017; Shkir et al. 2016b). From all the techniques applied to synthesize the nanostructure of  $\text{PbI}_2$ , the hydrothermal technique is

found to be the better one to have a well-organized nanostructure in the form of nanorods, nanoparticles, nanosheets, nanocrystals etc. The nanosynthesis of promising materials such as zinc oxide ( $\text{ZnO}$ ), titanium oxide ( $\text{TiO}_2$ ), bismuth telluride ( $\text{Bi}_2\text{Te}_3$ ), and tin oxide ( $\text{SnO}_2$ ) with cesium (Cs) doping using different techniques with tailored properties is already reported (Ragupathi et al. 2014; Kaviyarasu et al. 2012a; Mirabbaszadeh et al. 2013; Park et al. 2009; Srivastava and Singh 2014). These reports show that the key properties of any material can be controlled by Cs doping. According to the available literature, there is very popular Cs perovskite materials named  $\text{CsPbI}_3$  nanostructures (Luo et al. 2016). However, no report on the fabrication of low-concentration Cs-doped  $\text{PbI}_2$  nanostructures is available so far. Thus, herein, the authors plan is to fabricate the nanostructures of pure and low-concentration Cs-doped (1 to 10 wt%)  $\text{PbI}_2$  at low temperature with well-organized morphology using hydrothermal technique and characterize it to explore its possible applications in optoelectronic, room temperature radiation detection, and photocatalytic applications. The prepared nanostructures (nanorods and nanosheets) of the titled semiconductor may be useful in medical imaging, photovoltaics, sensors, solar cell, and photocatalytic applications, etc.

## Experimental

### Synthesis of pure and cesium-doped $\text{PbI}_2$ nanostructure

The high-purity lead acetate [ $\text{Pb}(\text{CH}_3\text{COO})_2$ ], sodium iodide (NaI), poly(vinyl alcohol) (PVA), cetyltrimethyl ammonium bromide (CTAB), and cesium nitrate ( $\text{CsNO}_3$ ) were bought from Alfa Aesar and Sigma Aldrich. For the synthesis of the aimed nanostructures, initially, 1 M lead acetate (39.987 g) was dissolved in 50 ml double-distilled water in a good quality and highly cleaned cylinder of 1000 ml volume, and after dissolving it, 50 ml CTAB solution (from the prepared solution with concentration of 50 g/l) and 50 ml of PVA (from the prepared solution with concentration of 10 g/l) were added to it one by one and stirred continuously to get a homogeneous solution at 300 K using a magnetic stirrer fixed at 1000 rpm. As it is acknowledged, the reaction media or surfactants play a central part in the synthesis of well-defined nanostructures of materials. Therefore, in the present work, CTAB and PVA both

are used as surfactants in order to organize the morphology of the subjected materials (AL-Thabaiti et al. 2013; Sabourimanesh et al. 2015). Step 2—2 M sodium iodide (37.795 g) was dissolved in 50 ml double-distilled water in a different beaker and stirred well with similar type of stirrer at the same rate. Homogeneous and transparent solutions were achieved through continuous stirring for 2 h, and both the above prepared solutions were mixed. Within few seconds of addition of sodium iodide solution (in lead acetate + CTAB + PVA solution), the transparent solutions become yellow which can be acknowledged to  $\text{PbI}_2$ . Similar procedure was done for preparing the other five solutions for doping purposes. In parallel to the above, we have prepared the solution of cesium nitrate for Cs doping (with different wt%, i.e., 1, 3, 5, 7, 10%) and added to the above product solution and continuously stirred. The finally achieved solutions were subjected to hydrothermal process. All the resulting products were subsequently transferred into indigenously designed Teflon-lined autoclave with a stainless steel shell for hydrothermal synthesis. All the autoclaves were housed in a well-controlled furnace at 145 °C temperature for 24 h and naturally cooled down to room temperature. The low-temperature hydrothermal synthesis of the well-organized nanostructures is well documented in the literature (Cheng et al. 2009; Pawar et al. 2010; Shkir et al. 2016b). The use of this technique was to achieve the nanostructures at low cost with good and arranged morphology facilely. The hydrothermally obtained yellow precipitates were washed several times with double-distilled water and filtered with high-quality Whatman filter paper and dried in vacuum at 80 °C for 4 h.

#### Characterization details

For structural as well as doping confirmations in all the fabricated nanostructures of pure and Cs-doped  $\text{PbI}_2$ , the powder X-ray diffraction (PXRD) patterns were recorded using a Shimadzu X-600 Japan powder X-ray diffractometer (PXRD) having  $\text{CuK}_\alpha$  radiation and wavelength  $\lambda = 0.1543$  nm and operated at 40 kV, 30 mA, at the scan rate of  $0.02^\circ/\text{m}$  over the angular range of  $5^\circ \leq 2\theta \leq 90^\circ$  at 300 K. The morphological and elemental analyses for all the prepared nanostructures were done by using a scanning electron microscope (SEM) (JSM 6360 LA, Japan) equipped with energy-dispersive analytical X-ray spectroscopy (EDAXS) unit. The prepared samples were sputter coated with 10-nm-

thick gold to get rid of the charge buildup during the SEM measurement. The vibrational study was carried out at room temperature for all the nanostructures using a FT-RAMAN and FT-IR spectrometer (Thermo Scientific, DXR) coupled with microscope using full-range grating ( $3500\text{--}100\text{ cm}^{-1}$ ). The Raman system was operated at 0.2 mW laser power (532 nm laser), and the estimated resolution and size of aperture pinhole was about  $5.1$  to  $8.3\text{ cm}^{-1}$  and  $50\text{ }\mu\text{m}$ , respectively. UV-Visible (UV-Vis) absorption measurement was carried out using a UV-Vis-NIR spectrophotometer (JASCO V-570) in the wavelength range from 190 to 1000 nm. Approximately 0.3 g of prepared nanostructures of pure and Cs-doped  $\text{PbI}_2$  has been taken for making its well organized pallets of same thickness about 2 mm. Before subjecting to the measurement, the prepared pallets were coated on both sides with platinum using a sputter system. Using a KEITHLEY 4200-SCS parameter analyzer, the dielectric constant, loss, and AC conductivity were analyzed in higher frequency range of 3 kHz–10 MHz at 300 K.

#### Photocatalytic activity measurement

Visible light photocatalytic activity measurements were conducted as described earlier in Hamdy et al. (2014) by using methyl green (MG) and methyl orange (MO) as model compounds under the illumination of visible light halogen tubes ( $\lambda > 425$  nm) as light source. Generally, three sets of experiments were conducted; in the first set, the photocatalytic activity of  $\text{PbI}_2$  was compared with commercially available photocatalysts (e.g.,  $\text{TiO}_2(\text{P}25)$ , ZnO, and  $\text{WO}_3$ ), while in the second set of experiments, the photocatalytic performance of  $\text{PbI}_2$  was compared with that of Cs-doped  $\text{PbI}_2$  by using MG and MO dyes in the third set. In a real experiment, 100 mg of the catalyst was introduced into the beaker with 50 ml of the applied dye (20 mg/L). The ultrasonication of solution was carried for approximately 10 min and kept inside a reactor, and stirring was done at 700 rpm for 15 min in the dark at room temperature to allow for chemisorption to occur. After this time had gone, a sample of this solution was taken, and the leftover solution was irradiated with visible light. Further samples were taken every 10 min, filtered through a 0.2-mm PTFE Millipore membrane, and lastly examined using the UV-Vis spectrometer in the range of 300 and 800 nm for MO and 400 to 800 nm for MG to determine the concentration of

the dye. The maxima at 631 and 468 nm were chosen to calculate the decolorization of MG and MO dye, respectively (Fig. 1). The reaction rate constant ( $K$ ) was then estimated assuming first-order kinetics using the following equation:  $\ln(C/C_0) = -Kt$ , where  $C_0$  is the initial concentration of the dye after the chemisorption,  $C$  is the concentration at time  $t$ , and  $K$  is the reaction rate constant.

## Results and discussion

### Structural analysis

Figure 2a shows the recorded diffraction patterns of the prepared nanostructures of pure and Cs-doped (1 to 10 wt%)  $\text{PbI}_2$ . The diffraction pattern sharpness confirms that the fabricated nanostructures possess good crystallinity. For the confirmation of single phase and its purity, crystalline structure, calculations of lattice parameters, and presence of doping, the recorded diffraction data was used as input in CHECKCELL software. The calculated cell parameters of pure and Cs-doped  $\text{PbI}_2$  are given in Table 1 and confirm that the prepared nanostructures are of high purity, single phase with hexagonal structure of space group P-3 m1, and found in great agreement with the earlier report (JCPDS-07-0235). After the close analysis of diffraction patterns, there is no extra diffraction peak that was observed due to  $\text{PbOHI}$  and  $\text{Pb}(\text{OH})_2$  impurities which further confirms its high purity. However, some peaks mainly in angular range from 20 to 35° with minute shifts with higher doping are present due to yellow orthorhombic

phase of  $\text{CsPbI}_3$  in all the doped structures (JCPDS-74-1970). From this, it may also be concluded that by higher concentration of Cs doping in  $\text{PbI}_2$ , the non-perovskite phase is also formed (Eperon et al. 2015; Luo et al. 2016). From the indexed diffraction patterns, it is clear that the prepared nanostructures are of 2H-polytype of  $\text{PbI}_2$  predominantly. The variation of lattice parameters such as  $a$ ,  $c$ , and  $V$  are shown in Fig. 2b. From the figure, it can be concluded that Cs has a strong effect on the lattice of  $\text{PbI}_2$ . The value of  $a$  and  $V$  is found to be increased up to 7 wt% Cs doping; however, at 10 wt% Cs doping, it reduces but still higher than pure, 1 and 3 wt% Cs doped  $\text{PbI}_2$ .

Moreover, on comparing the predominant peak in the diffraction patterns (Fig. 2c), a clear slight shift in peak positions towards the lower as well as higher angles was observed which suggest Cs doping in the  $\text{PbI}_2$  matrix. Furthermore, the crystallite size of the fabricated pure and Cs-doped  $\text{PbI}_2$  nanostructures was estimated by using the well-known Scherer's formula:  $D = \frac{k\lambda}{\beta \cos\theta}$ , where  $k = 0.9$  and  $D$ ,  $\lambda$ , and  $\beta$  are known as average crystallite size, X-ray wavelength (0.1543 nm), and full width at half maximum in radian, respectively. For all the prepared nanostructures, the determined values of crystallite size are presented in Table 1. Values of strain ( $\epsilon$ ) and dislocation density ( $\delta$ ) were also calculated (given Table 1) from the following relations:  $\epsilon = \frac{\beta \times \cos\theta}{4}$ ,  $\delta = \frac{15\epsilon}{a \times D}$ . No systematic variation in crystallite size, strain, and dislocation was observed with doping. The value of crystallite size was found to be in the range of 46–64 nm. The value of crystallite size is found to be decreased with Cs doping. Similarly, results were observed in Cs-doped  $\text{SnO}_2$  (Kaviyarasu et al. 2012a).

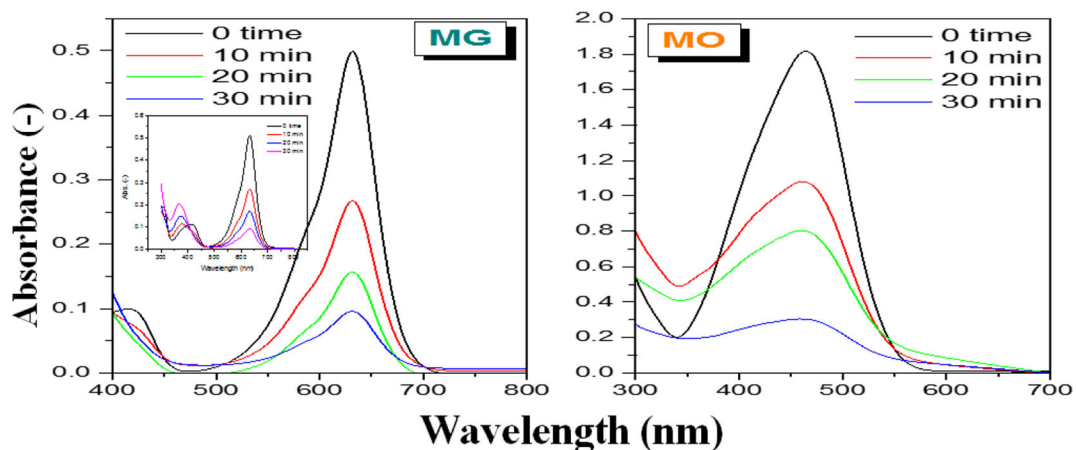


**Fig. 1** The UV-Vis spectra of MG (left panel) and MO (right panel) during real photocatalytic reactions catalyzed by  $\text{CsPbI}_2$

The decrease in crystallite size may be due to the small grain growth of Cs-doped  $\text{PbI}_2$  nanorods and nanosheets as compared to pure  $\text{PbI}_2$ . This may also be due to the different size of radii of the dopant in comparison to the parent matrix which affects the strain or stress field that disturbs the process of grain growth.

EDAXS and SEM analyses

To study the effect of dye doping on the morphology of nanostructures as well as to know the presence of dopant and elemental composition, the synthesized powders were subjected to SEM/EDAXS analysis. Figure 3a (a–e) shows the recorded EDAXS patterns of pure and Cs-doped  $\text{PbI}_2$  nanostructure. From Fig. 3a (b–e), it is clear that Cs ions are present in the synthesized  $\text{PbI}_2$  nanostructures. The % of Cs was found to be ~ 0.40, 0.90, 1.4, 1.8, and 2.1, respectively. Further, the SEM micrographs of pure and (1, 3, 5, 7, and 10%) Cs-doped

$\text{PbI}_2$  nanostructures synthesized by hydrothermal technique under the similar conditions were captured at different places of each specimen and are shown in Figs. 3b and 4. From Fig. 2a, b, it is clear that the synthesized nanostructures are of well-aligned nanorods and the morphology has not been much affected by 1 wt% Cs doping. In 3 wt% Cs-doped nanostructures (Fig. 3b (c)), the few nanosheets appear with a large number of nanorods. However, from Fig. 4a, b, it is clear that the synthesized nanostructures are only nanosheets at higher concentrations, i.e., 5, 7, and 10 wt%. The density of nanosheets is more at 5 and 7 wt% Cs doping (Fig. 4); however, at 10% Cs doping (Fig. 4c), the nanosheets become low dens and cover large area. This means that higher-concentration Cs doping has a strong effect on the morphology of  $\text{PbI}_2$ .

The average diameter of the fabricated nanorods is within the range of ~ 100 nm with few micrometer length for pure to 3% Cs and the average thicknesses

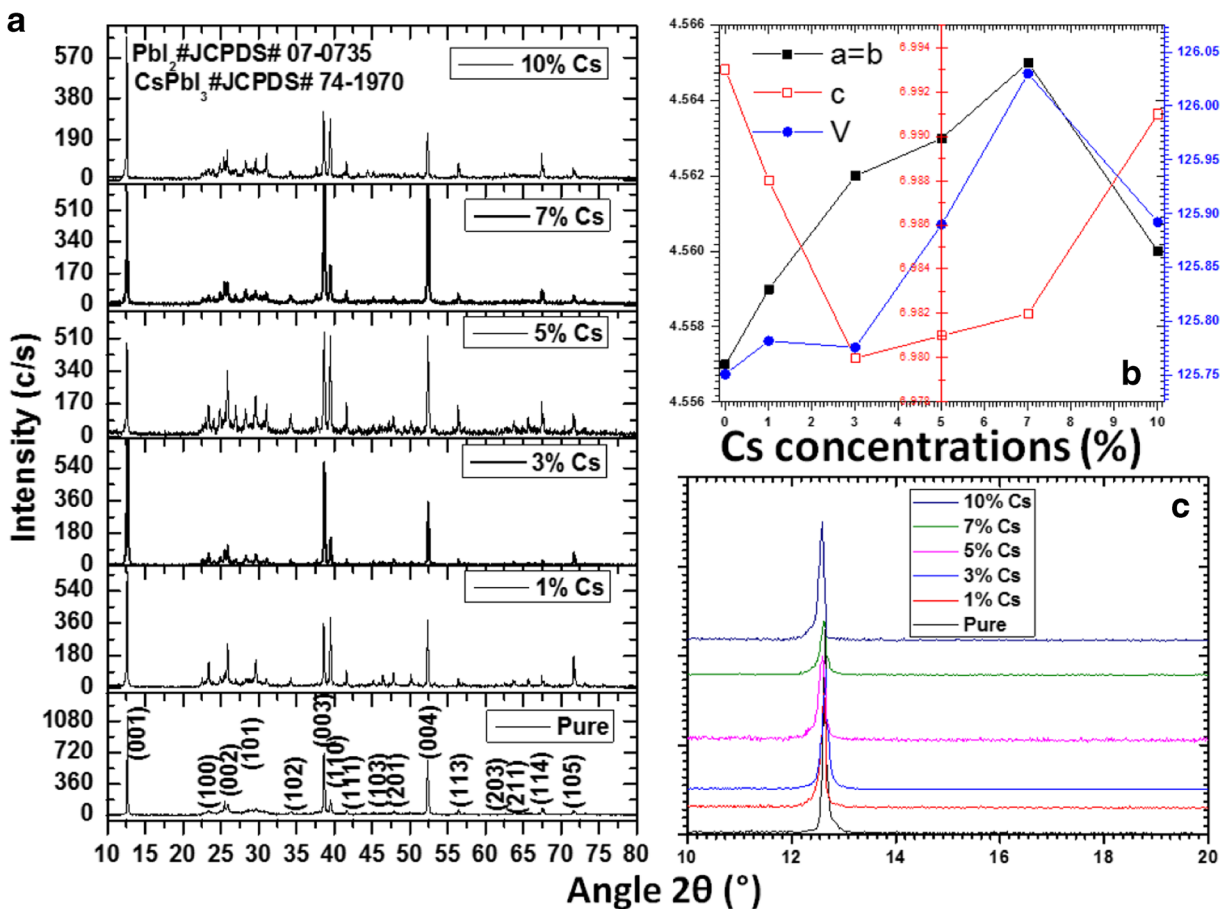


Fig. 2 a Powder X-ray diffractions pattern. b Variation of lattice parameters c Close view of main diffraction peak

**Table 1** Lattice parameters of pure and Cs-doped PbI<sub>2</sub> nanorods and nanosheets refined by POWDERX software

Sample	a = b (Å)	C (Å)	V (Å) <sup>3</sup>	D (nm)	$\epsilon \times 10^{-4}$	$\delta \times 10^{-4}$ (nm <sup>-2</sup> )
JCPDS#7-0235	4.557	6.979	125.511	–	–	–
P	4.557	6.993	125.751	63.73025	3.05095	5.902
1 wt% Cs	4.559	6.988	125.782	57.28638	3.04717	6.645
3 wt% Cs	4.562	6.980	125.776	57.05917	3.29588	6.211
5 wt% Cs	4.563	6.981	125.890	56.27597	3.85515	6.624
7 wt% Cs	4.565	6.982	126.030	52.43670	4.10971	6.879
10 wt% Cs	4.560	6.991	125.892	46.54233	5.00420	7.654

of nanosheets may be in the range of ~ 20–40 nm with few microns of length at higher concentration of Cs doping with well-defined morphology. The size of the nanorods is found to be minutely decreased with Cs doping and evolving to nanosheets at higher-concentration doping. The morphological evolution from nanorods to nanosheets may possibly be due to the fact that the Cs ions could disturb the PbI<sub>2</sub> crystal lattice and obstruct the growth process; however, no secondary phase was observed on the surface of the sheets. The formation of nanorods is well documented using different techniques (Barnakov et al. 2001; Kaviyarasu et al. 2012b; Shkir et al. 2016a; Zhu et al. 2007a); however, very recently, the nanosheets were synthesized by our group in presence of Gd<sup>3+</sup> doping in PbI<sub>2</sub> (Shkir et al. 2017; Shkir et al. 2016b). These results show that the higher concentration of Cs doping has strong effect on the morphology of PbI<sub>2</sub> nanostructures.

#### FT-Raman analysis

Figure 5 shows the recorded FT-Raman spectra for single crystal grown by gel method (Henisch 1996) as well as hydrothermally prepared pure and Cs-doped PbI<sub>2</sub> nanostructures. The Raman spectra of pure and Cs-doped PbI<sub>2</sub> nanostructures confirm the high purity of the prepared system which is in good correlation with X-ray diffraction analysis. The intensity of Raman peaks is found to be enhanced at 3 wt% Cs doping concentrations which is a mixture of nanorods and nanosheets; however, at other concentrations, it was found to be continuously reduced. The reduction of intensity at higher concentration clearly indicates the reduction in crystallinity of the prepared nanostructures which is also confirmed by the low crystallite size determined by X-

ray diffraction study. However, the intensity of Raman peaks is quite good to have an idea about the crystallinity of the prepared nanostructures. As clear from the figure that the Raman spectrum have visible and strong Raman bands at ~ 75, 100, 115, 170, and 220 cm<sup>-1</sup> in pure; at 75, 100, 115, 171, and 218 cm<sup>-1</sup> in 1 wt% Cs; at 75, 100, 115, 171, and 218 cm<sup>-1</sup> in 3 wt% Cs; at 75, 100, 114, 172, and 220 cm<sup>-1</sup> in 5 wt% Cs; at 75, 100, 115, 170, and 221 cm<sup>-1</sup> in 7 wt% Cs; and at 76, 100, 115, 171, and 219 cm<sup>-1</sup> in 10 wt% Cs. The other bands are also present in all the recorded spectra with low intensity and peak broadness. Our results were compared with the reported bands for bulk 2H-PbI<sub>2</sub> and 4H-PbI<sub>2</sub> polytype crystals and nanoparticles (Kasi et al. 2007; Khilji et al. 1982; Sears et al. 1979; Sengupta et al. 2000), which were attributed as vibration modes of E<sub>2</sub><sup>1</sup>, A<sub>1</sub><sup>1</sup>, A<sub>1</sub><sup>2</sup>, 2E<sub>2</sub><sup>1</sup>, and 2E<sub>1</sub><sup>1</sup>, respectively (Baltog et al. 2009; Sears et al. 1979; Sengupta et al. 2000). The more detail on Raman study on bulk PbI<sub>2</sub> crystal with six polytypes can be seen somewhere else (Sears et al. 1979). Raman bands predominantly for 2H-PbI<sub>2</sub> polytypes along with few bands of 4H-PbI<sub>2</sub> polytypes were observed which is in good correlation with our X-ray diffraction study. The vibration bands in grown single crystal are observed at ~ 80.91, 104.05, 118.5, 176.1, and 223.6 cm<sup>-1</sup> (see inset of Fig. 5). Hence, the clear shifting in the Raman bands are observed between crystals and nanostructures fabricated in the present work. The clear shifting in the Raman bands towards the lower wavenumber is observed for the synthesized nanorods as well as nanosheets in comparison of bulk crystals which may be accredited to relaxed binding in synthesized nanostructures due to their larger surface-to-volume ratio. Such shifting in the vibrational bands was also observed in the previous report on nanoparticles, nanocrystals, and nanorods (Kasi et al. 2007). It is clear from Raman

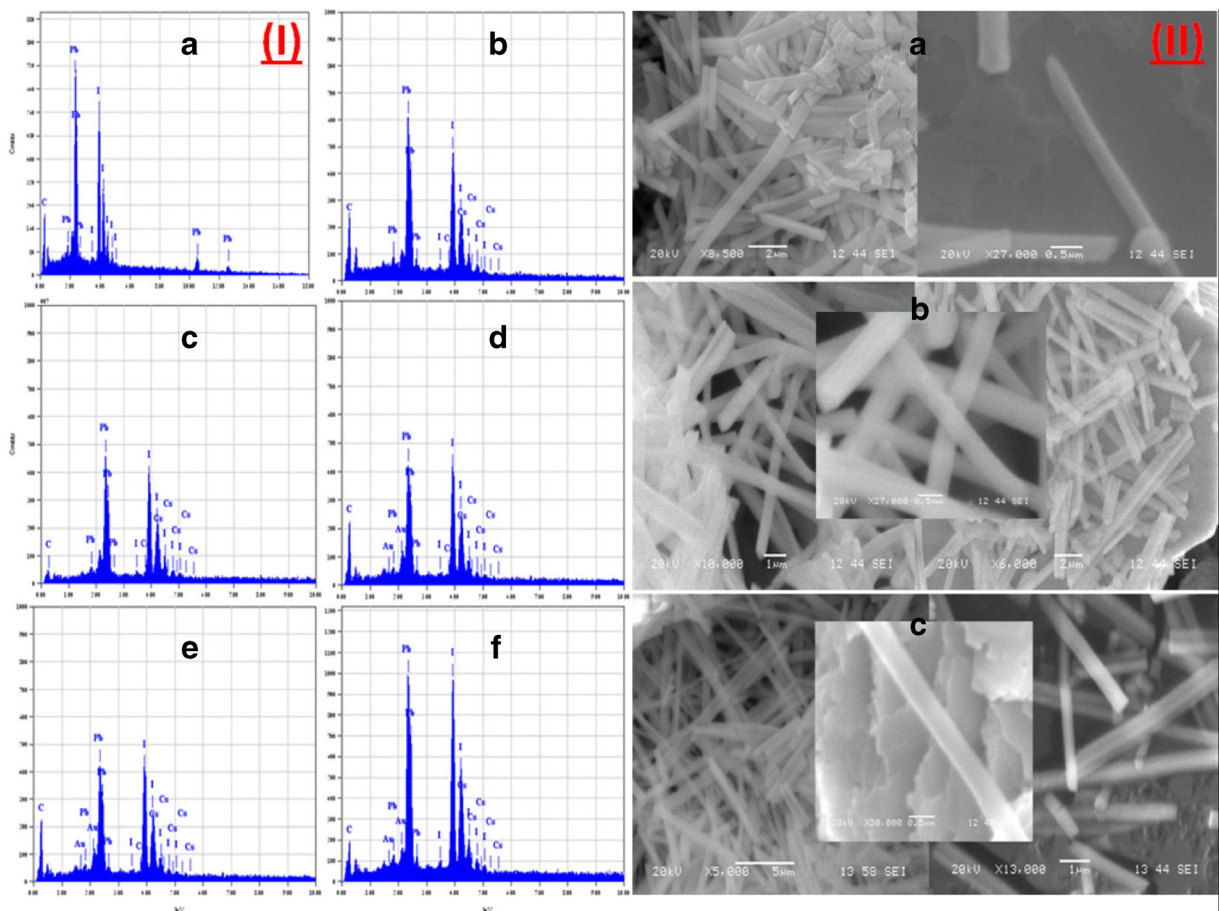


**Fig. 3** a EDS patterns of (a) pure and (b) 1 wt%, (c) 3 wt%, (d) 5 wt%, (e) 7 wt%, and (f) 10 wt% Cs doped and b SEM micrographs of (a) pure and (b) 1 wt% and (c) 3 wt% Cs-doped  $PbI_2$  nanorods

spectra that the fabricated nanostructures are highly crystalline in nature. It may be mentioned here that one may expect the additional peaks in the Raman spectra due to another phase as mentioned in the XRD section. However, due to the dominant nature of main phase formation of  $PbI_2$ , no additional peaks were detected in the fabricated doped nanostructures (Shkir et al. 2016b) except a shift in the peak position.

Optical band gap analysis

Figure 6a shows the recorded absorbance spectra for pure and Cs-doped nanostructures. The absorbance spectra were recorded for colloidal solutions prepared in methanol as solvent. For calculating the energy gap, the Tauc’s relation was used and the Tauc’s plot is shown in Fig. 6b. Further, to obtain the energy gap from the Tauc’s plot, one-line straight line has been extrapolated to curve  $(\alpha h\nu)^2$  vs.

$h\nu$ , to the point of intersection where  $(\alpha h\nu)^2 = 0$  with energy axis, and  $h\nu$  and  $\alpha$  are known to be photon energy and absorption coefficient. The absorption coefficient  $\alpha$  was calculated from the very well-known Beer–Lambert relation,  $\alpha = 2.303 A/R$ , where  $A$  is UV-Vis absorbance and  $R$  is the path length of the used quartz cuvette (10 mm) in this measurement. The optical band gap for pure and Cs-doped nanostructures is found to be in the range of 3.287–3.427 eV. The calculated band gap is found to be remarkably enhanced for the prepared nanostructures compared to the bulk value of  $PbI_2$ , i.e., 2.27 eV (Zhu et al. 2007b). The enhancement in the value of band gap may be due to the Cs doping as well as quantum confinement effect. It is also in correlation with crystallite size which is found to be reduced with doping. In previous reports, the value of the band gap of  $PbI_2$  nanostructures is reported to be 2.85 eV (Kaviyarasu et al. 2012b) and 3.84 eV (Chakrabarty et al. 2014). However, previously reported values of band gap

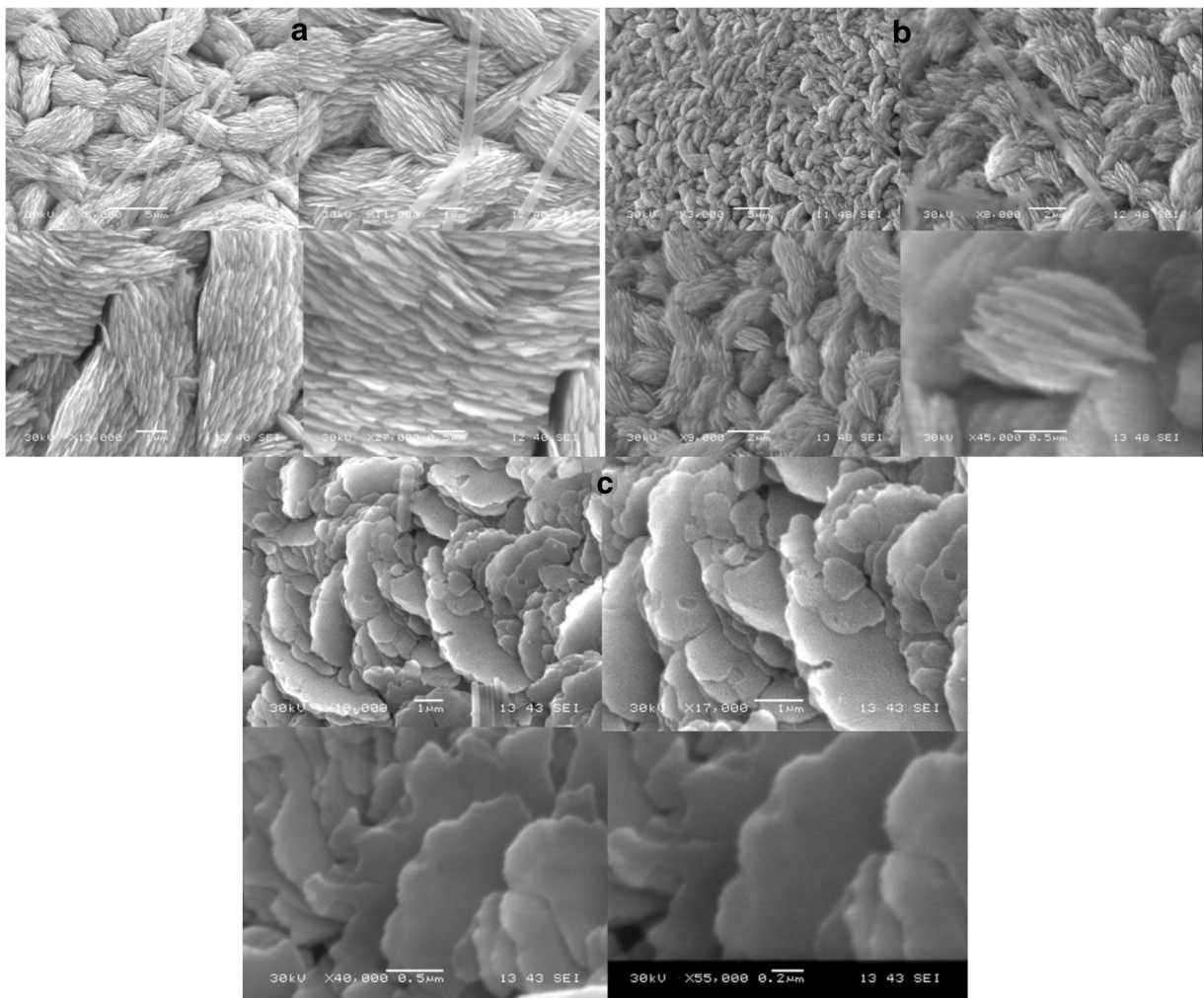


**Fig. 4** SEM micrographs of bundles **a** 5 wt%, **b** 7 wt%, and **c** 10 wt% Cs-doped  $\text{PbI}_2$  nanosheets

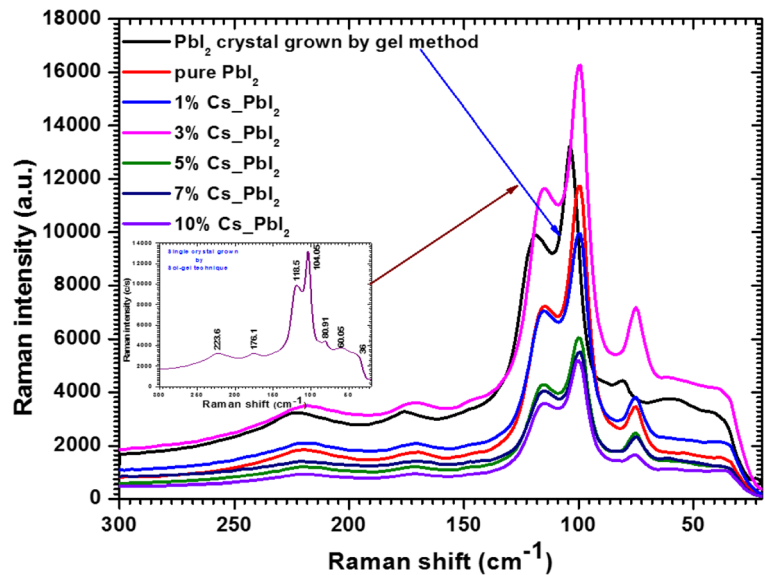
calculated from diffused reflectance also have differences and are comparable as both techniques are fully different. The results obtained in UV-Vis study are more expected for pure as well as doped  $\text{PbI}_2$  nanostructures than in DR study (Kaviyarasu et al., 2012a, Chakrabarty et al., 2014). From these studies, we conclude that the UV-Visible techniques is better for semiconductor nanostructured materials especially for  $\text{PbI}_2$  as by doping, it is not easy to change the color of it as it is a deep yellow material and will not give proper results in DR analysis which gives the same reflected data from the surface (i.e., DR technique is for color change material measurement). It can also be considered for our previous articles on doped  $\text{PbI}_2$  in which we have provided DR analysis as the results may be different when we go to study them by UV-Vis data (Shkir et al., 2016a, Shkir et al., 2017).

#### Dielectric and electrical analysis

The dielectric measurement on pure and Cs-doped  $\text{PbI}_2$  nanostructures synthesized by hydrothermal technique has been carried out in the high frequency range, i.e., 3 kHz to 10 MHz at 300 K. Figure 7a, b shows the plots of variation of dielectric constant,  $\epsilon_1 = \frac{C \times l}{\epsilon_0 \times A}$ , (where  $\epsilon_0$  is the permittivity of space,  $A$  is the area of electrode,  $C$  is capacitance, and  $l$  is thickness of the prepared pallets) and dielectric loss,  $\epsilon_2 = \tan \delta \times \epsilon_1$ , (where  $\tan \delta$  is loss tangent) vs. frequency. From Fig. 7a, it is clear that the  $\epsilon_1$  values are higher in the lower-frequency range and become almost constant at larger frequencies. The behavior of dielectric constant in the low frequency range is due to all four charges such as electronic, ionic, dipolar, and space charge polarizations because they



**Fig. 5** FT-Raman spectra of pure and Cs-doped PbI<sub>2</sub> nanostructures



depend on the frequencies (Xue and Kitamura 2002). The  $\epsilon_1$  value for pure and Cs-doped nanostructures is observed to be lessened with frequency and turn out to be nearly stable between 1 and 6 MHz, which depends on the fact that the electric field dipole does not follow the alternating field beyond a certain frequency (Batra et al. 2005; Hill 1969; Shakir et al. 2010; 2009a; 2009c). The value of  $\epsilon_1$  of the fabricated nanostructures of pure as well as Cs-doped PbI<sub>2</sub> is found to be higher compared to bulk PbI<sub>2</sub> single crystal at 293 K (Dugan and Henisch 1967; Glasser et al. 1967; Hassan et al. 2010). It can be seen that the value of  $\epsilon_1$  is found to be reduced by Cs doping which may be due to interfacial charge transfer. Similar type of results was reported previously on Nd-

and Sm-doped TiO<sub>2</sub> and Cs-doped SnO<sub>2</sub> as well (Gafoor et al. 2013; Gafoor et al. 2011; Kaviyarasu et al. 2012a). Decrease of the  $\epsilon_1$  value with Cs substitution in the lower frequency range is observed due to the smaller grain size that has different polarization mechanism. In the present work, Cs doping may be increasing the grain boundaries on PbI<sub>2</sub> that cause the reduction in polarization and hence the values of  $\epsilon_1$  (Gafoor et al. 2013; Koops 1951). The decrease in the value of dielectric constant of Cs-doped PbI<sub>2</sub> nanostructures validates that the fabricated nanostructures will have low electrical power consumption which is a critical factor in fabricating and designing the photonics, microelectronics, broad band electro-optic modulators, field detectors,

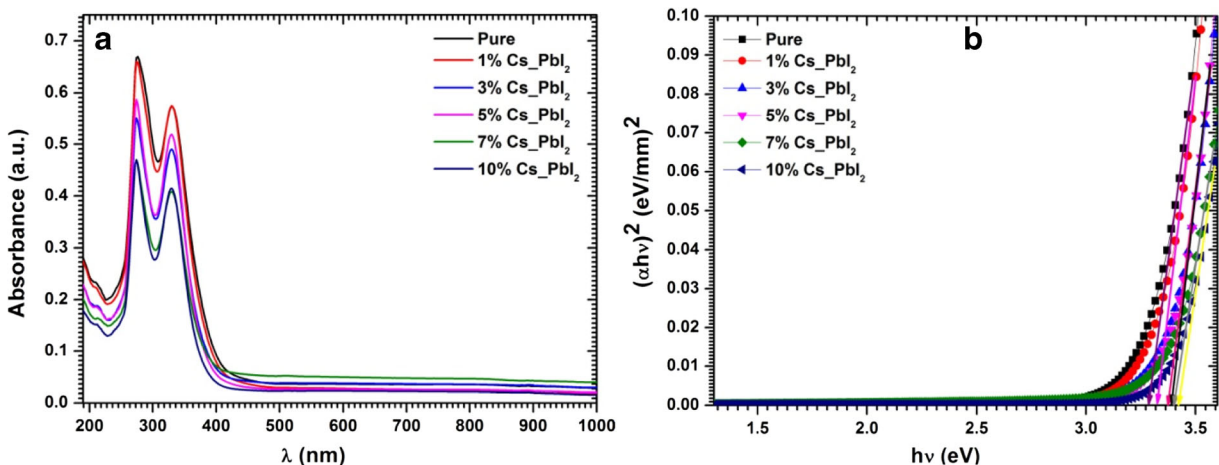


**Fig. 6** **a** UV-Vis spectra and **b** energy band gap determination plot

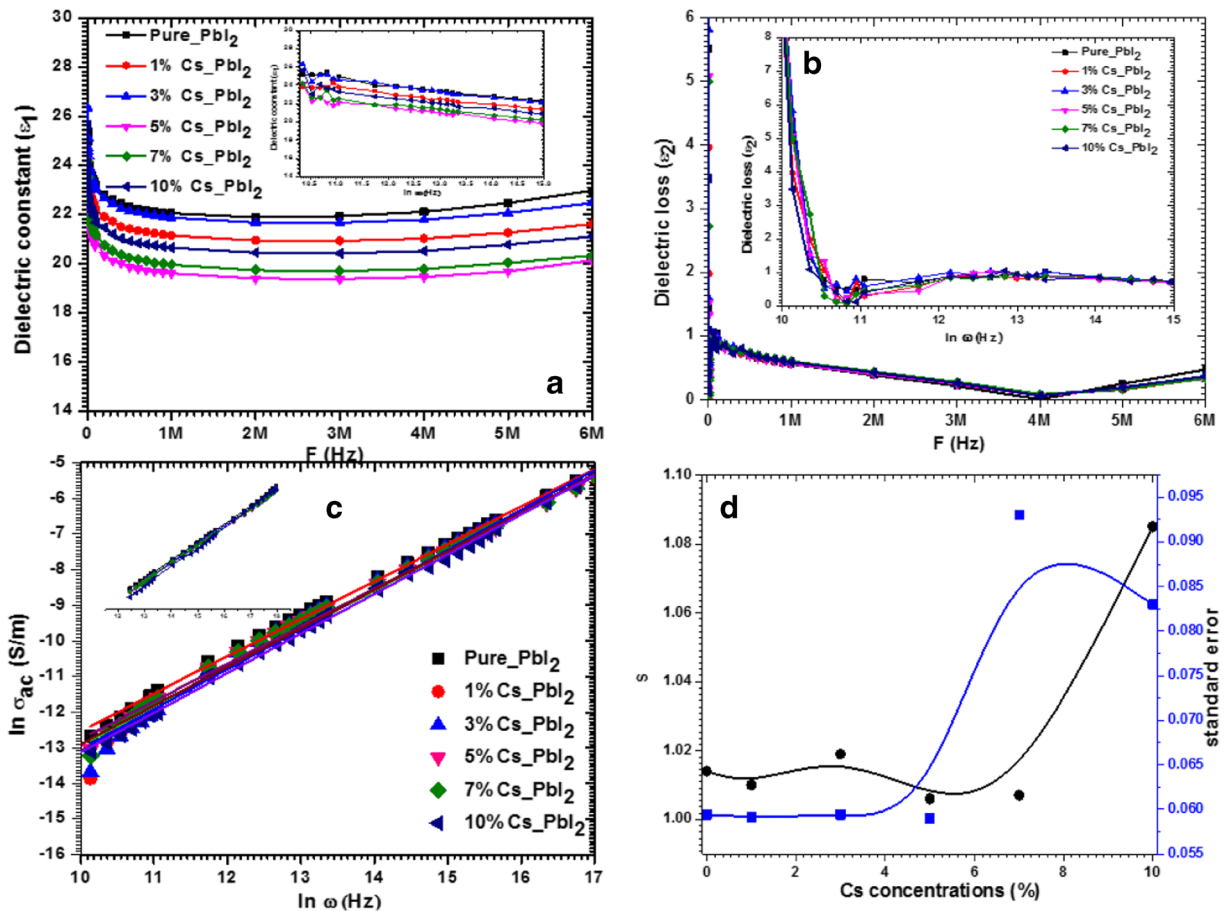


**Fig. 7** Plots of variation of **a** dielectric constant and **b** dielectric loss and **c** ac conductivity as a function of frequencies and **d** frequency exponent with Cs concentration

and THz wave generators (Anis et al. 2016; Shanmugam et al. 2013). The dielectric loss was also found to have similar behavior as dielectric constant and dependent on the frequency as shown in Fig. 7b. Further, the total alternating current conductivity ( $\sigma_{ac, tot.}$ ) was determined by the following relation:  $\sigma_{ac, tot.} = \frac{I}{Z \times A}$ . For the determination of conductivity mechanism, we have applied the well-known Jonscher law:  $\sigma_{ac} = \sigma_{dc} + B\omega^s$ , where  $\sigma_{dc}$  is the direct current conductivity,  $B$  is a constant,  $\omega$  is angular frequency, and  $s$  is an exponent. The calculated ac conductivity ( $\sigma_{ac, tot.}$ ) plot of variation with frequency for all the synthesized nanostructures has been shown in Fig. 7c. It is clear from the figure that the  $\sigma_{ac}$  is found to increase with increase of the frequency and obeys the universal frequency power law behavior. However, the ( $\sigma_{ac}$ ) was found to be decreased with addition of Cs dopant in PbI<sub>2</sub> matrix. The value of  $s$  was also calculated for all the specimens from the slope of  $\ln \sigma_{ac}$  vs.  $\ln \omega$  and found to be

1.049, 1.071, 1.122, 1.054, 1.066, and 1.110 with standard error 0.109, 0.160, 0.248, 0.135, 0.152, and 0.080 for pure, 1 wt% Cs, 3 wt% Cs, 5 wt% Cs, 7 wt% Cs, and 10 wt% Cs-doped PbI<sub>2</sub> nanostructures, respectively. However, the values of  $s$  calculated from the linear part of the curve for all the nanostructures are as follows: 1.014, 1.010, 1.019, 1.006, 1.007, and 1.085 with standard error 0.0594, 0.0591, 0.0594, 0.0590, and 0.093 for pure, 1 wt% Cs, 3 wt% Cs, 5 wt% Cs, 7 wt% Cs, and 10 wt% Cs-doped PbI<sub>2</sub>. The variation in the value of  $s$  with Cs concentration is shown in Fig. 7d. Its values are frequency dependent and it is about 1. Generally, the value of  $s$  is reported between 0.6 and 1 for ionic conducting materials (Lee et al. 1991) and the theoretical limit of it is about 1. The  $n$  value has a physical significance or explanation that if  $n \leq 1$  then the hopping motion involves a translation motion with a sudden hopping whereas if  $n \geq 1$ , the hopping motion involves localized hopping. As clear from the present study, the

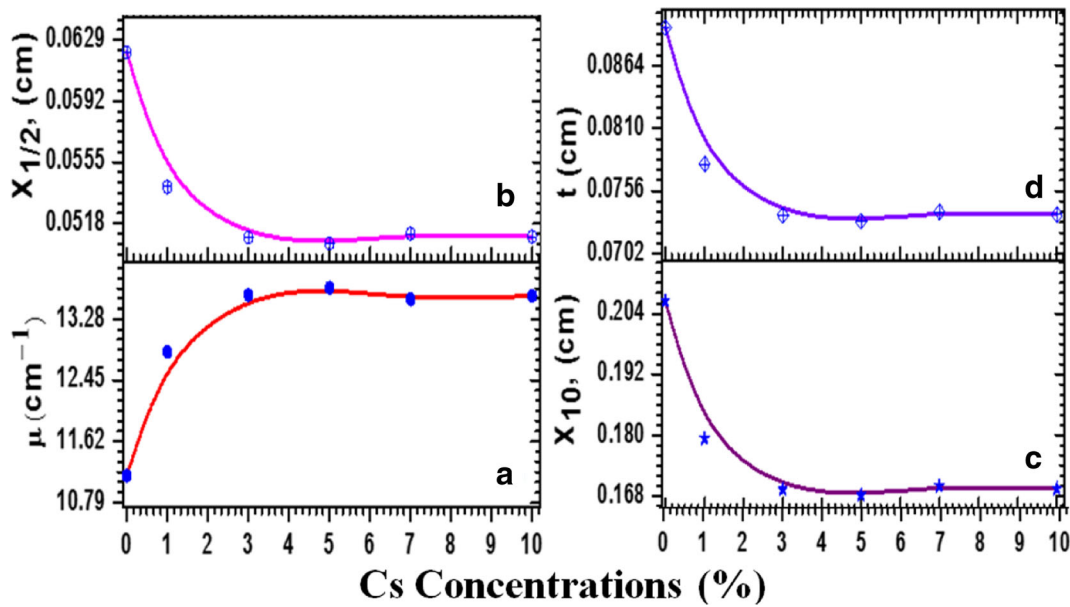


**Fig. 8** Plots of variation of **a** linear attenuation coefficient, **b** half value layer, **c** tenth value layer, and **d** mean free path vs. Cs concentrations

value of  $s$  is about 1 when calculated from the linear part of the curve for all the prepared nanostructures. The case of  $s > 1$  was also observed and reported previously in some crystalline compositions, semiconductors, and glasses 1 (Chen et al. 2000; El-Mallah 2012; El-Mallah and Hegab 2007; Le Stanguennec and Elliott 1994).

Photon linear attenuation coefficient study

The nanostructurization of high atomic number ( $Z$ ) materials are the key for medical radiology, high resolution, and real-time radiation detectors (Nambiar et al. 2015; Nambiar and Yeow 2012; Retif et al. 2015). It is well

known that the unwanted exposures to ionizing radiation or high energy can be hazardous to human health (Bushberg and Boone 2011; Nambiar and Yeow 2012). The linear absorption or attenuation coefficients help to understand how the interaction of Gamma photon takes place with materials.  $PbI_2$  contains lead which has high density and atomic number and absorbs much higher fraction of gamma radiation than the aluminum and steel of the same thickness. As  $PbI_2$  is already a well-known radiation detector, the authors believe that by adding another metal as dopants will increase the radiation ability of these materials and hence chose these materials for radiation measurement. Therefore, it is

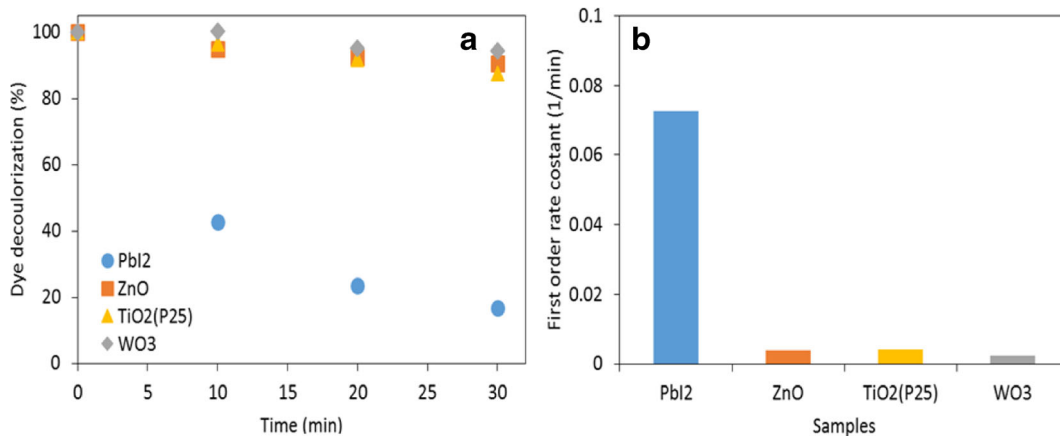


**Fig. 9** **a** The photocatalytic decolorization of MG in the presence of  $PbI_2$  compared with other commercially available photocatalysts and **b** the first-order rate constant of the corresponding decolorization profiles

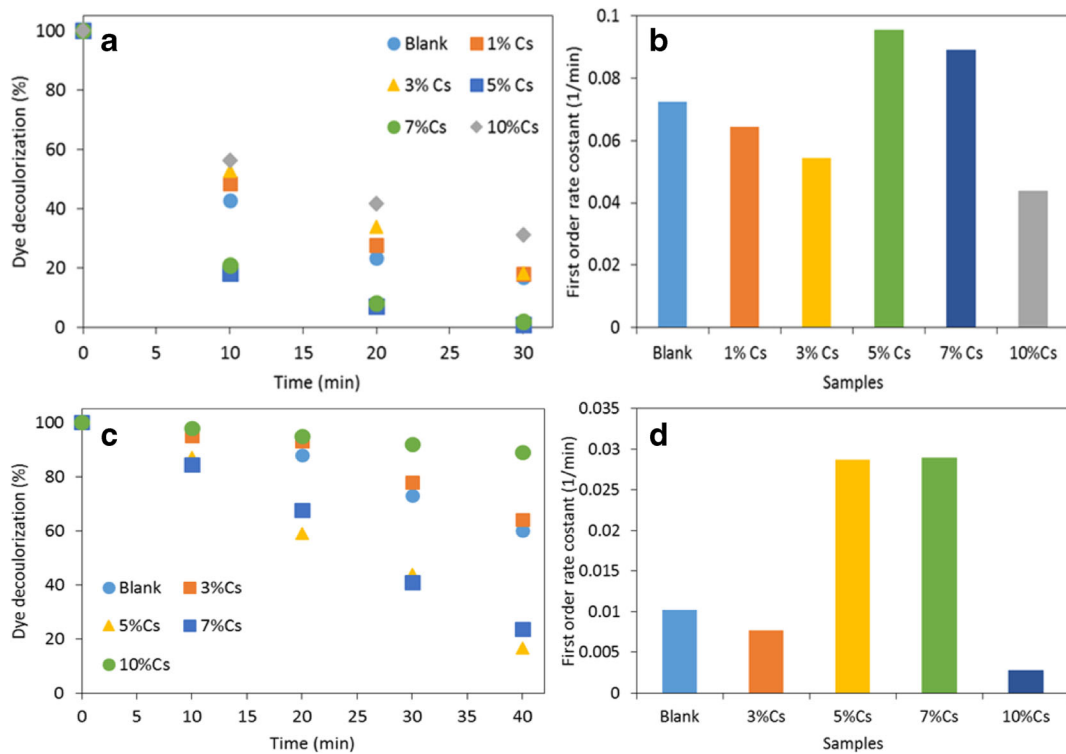


**Fig. 10** **a** The decolorization profiles of MG dye catalyzed by the different prepared samples of Cs-doped  $\text{PbI}_2$  and **b** the corresponding first-order rate constants. **c** The decolorization profiles of MO

dye over Cs- $\text{PbI}_2$  samples and **d** the corresponding first-order rate constants of the investigated catalysts

important to study the gamma radiation absorption properties of  $\text{PbI}_2$  for applications in science, technology, agriculture, and human health (Zentai et al. 2005). In the present work, we have measured the absorption properties of the fabricated nanostructures of pure and Cs-doped  $\text{PbI}_2$  using a single AM-241 [ $(I_o)_{\text{avg.}} = 68,774$  (59.5 keV)] radiation source at room temperature (the pallets of same thicknesses were prepared). For calculating the linear attenuation coefficient, the fundamental law of Gamma-ray attenuation has been used and the expression is given as follows:  $I = I_o e^{-\mu_l x}$ , where  $I_o$  is the intensity of radiation counted during a certain time duration without any absorber,  $I$  is the intensity counted during the same time with a thickness  $x$  of absorber (pure and Cs doped  $\text{PbI}_2$  samples) between the source of radiation and the detector, and  $\mu_l$  is the linear attenuation coefficient. The plots of variation of  $\mu_l$  values vs. Cs concentrations have been shown in Fig. 8a. It is clear from the figure that the value of  $\mu_l$  has been enhanced from 10.956 for pure  $\text{PbI}_2$  to 13.612 for 10 wt% Cs-doped  $\text{PbI}_2$ ; however, at higher concentration, it becomes steady. This value is very high and also

comparable with other studied materials (Burger et al. 2002; Hubbell 1982) and confirms that  $\text{PbI}_2$  is highly applicable as a room temperature radiation detector. Further, there are other important parameters such as half value layer (HVL) of half-value thickness  $x_{1/2}$ , tenth value layer (TVL) ( $x_{1/10}$ ), and mean free path ( $t$ ) known as the average distance to travel in the absorber by Gamma ray before interacting. The  $x_{1/2}$  is known as the thickness of absorber which needs to reduce the intensity of a incident photon beam to one-half of its initial value; it can be calculated from the following procedure [43]:  $\frac{I}{I_o} = e^{-\mu_l x / t}$ , by solving the above equation,  $x_{1/2}$  will be as  $x_{1/2} = \frac{\ln 2}{\mu_l}$ . The calculated value of  $x_{1/2}$  vs. Cs concentrations is shown in Fig. 8b, and it is clear that the value of half value layer is decreasing with Cs doping. In the same way, the tenth-value layer  $x_{1/10}$  will be as  $x_{1/10} = \frac{\ln 10}{\mu_l}$ . The determined values of  $x_{1/10}$  is found to be decreased with Cs concentrations as shown in Fig. 8c. The value of mean free path was also calculated by  $t = 1/\mu_l$ , and the plots of variation of  $t$  with Cs concentration is shown in Fig. 8d.

## Photocatalytic activity

Three batches of photocatalytic experiments were carried out; in the first batch, the photocatalytic performance of the prepared  $\text{PbI}_2$  was compared with that of the commercially available photocatalysts such as  $\text{TiO}_2$  (P25),  $\text{ZnO}$ , and  $\text{WO}_3$ . The photocatalytic performance of the four samples is presented in Fig. 9a, b. It is clearly seen that  $\text{PbI}_2$  is the most active material under the illumination of 425 nm. The observed reaction rate is almost ten times higher than the other commercially available photocatalysts studied in current work for comparison.  $\text{TiO}_2$  and  $\text{ZnO}$  do not have an excitation bands in the visible light, so the observed results were expected. Surprisingly,  $\text{WO}_3$  did not show a photocatalytic performance although  $\text{WO}_3$  has an adsorption band in the illumination area; the reason for such behavior needs further investigations.

In the second batch, the photocatalytic performance of the  $\text{PbI}_2$  was compared to that of Cs-doped  $\text{PbI}_2$  (Fig. 10a–d). From the obtained results, the samples with a lower loading of Cs (1 and 3 wt%) and that with a higher loading (10 wt%) do not seem to have any positive effect on the photocatalytic activity of  $\text{PbI}_2$ , and the photocatalytic activity of  $\text{PbI}_2$  was found to be decreased with the above-mentioned Cs loading. Such reduction in photocatalytic activity was also observed for Cr- and Mo-doped  $\text{TiO}_2$  which are known to be efficient photocatalysts even at their higher doping concentrations (Rauf et al. 2011; Wilke and Breuer 1999). However, at 5 and 7 wt% Cs loading in  $\text{PbI}_2$  shows a very strong photocatalytic activity under the visible light illumination compared to other. The samples with 5 and 7 wt% Cs loading showed 15–20 wt% higher photocatalytic activity than the pure  $\text{PbI}_2$ . Such enhancement in photocatalytic activity may be due to more compact nanostructures in the form of rough bundles of nanosheets with high surface area compared to nanorods of  $\text{PbI}_2$  compared to other which can be seen in SEM.

## Conclusions

Pure and Cs-doped  $\text{PbI}_2$  nanostructures have been fabricated successfully by hydrothermal route at low temperature with good quality and well-defined morphology. The structural and vibrational studies authenticate the production of a 2H- $\text{PbI}_2$  polytypic with hexagonal structure. The clear shift in the Raman bands was observed towards lower wavenumber with

respect to bulk values which may be attributed to extra stress-free binding due to their larger surface-to-volume ratio. The pure and 1 and 3 wt% Cs-doped fabricated nanostructures are nanorods of average diameter about  $\sim 100$  nm with length of few microns; however, at higher concentration doping of Cs, the fabricated nanostructures are found to be nanosheets of average thickness in the range of  $\sim 20$ – $40$  nm and size of few microns with well defined morphology as confirmed by SEM. Different morphologies for  $\text{ZnO}$  and  $\text{PbS}$  were also reported via polymeric complex prepared via sol-gel and hydrothermal process (Farhadi-Khouzani et al. 2012; Mohammadikish et al. 2015). The optical band gap for pure and Cs-doped nanostructures is found to be in the range of 3.287–3.427 eV, which is higher than the bulk value (i.e., 2.27 eV). Such enhancement in the value of band gap may be due to Cs doping as well as quantum confinement effect. The high band gap of the pure and Cs-doped  $\text{PbI}_2$  suggests its applications in optoelectronic devices which can be utilized at higher voltages, frequency, and temperature than usual semiconductor materials. This may allow us for an extra influential electrical system to be manufactured with low cost and high energy efficiency (Casady and Johnson 1996; Chow and Tyagi 1994; Feng et al. 2004; Kirschman 1999; Periyasamy et al. 2007; Shakir et al. 2009b; 2012a; 2014; Vavilov 1994; Vogel et al. 1994). Relative permittivity, dielectric loss, and ac conductivity are found to be varied with increasing the frequency and gradually decrease with Cs doping. The enhancement in the values of Gamma linear absorption coefficient is observed with Cs doping. High photocatalytic response under the illumination of visible light was observed for 5 and 7 wt% Cs-doped  $\text{PbI}_2$ , and the recorded activity is ten times larger compared to commercially available photocatalysts. All the results suggest that the fabricated nanostructures can be suitable in various optoelectronic device applications.

**Acknowledgements** The authors extend their appreciation to the Deanship of Scientific Research at King Khalid University for funding this work through research group program under grant number R.G.P.2/3/38.

## Compliance with ethical standards

**Conflict of interest** The authors declare that they have no conflict of interest.

## References

- Ahn Y, Jeong Y, Lee D, Lee Y (2015) Copper nanowire–graphene core–shell nanostructure for highly stable transparent conducting electrodes. *ACS Nano* 9:3125–3133. <https://doi.org/10.1021/acsnano.5b00053>
- Albrecht M, Green M (1977) The kinetics of the photolysis of thin films of lead iodide. *J Phys Chem Solids* 38:297–306
- AL-Thabaiti SA, Obaid AY, Khan Z (2013) Synthesis of Poly (vinyl alcohol)-silver nanocomposites and effect of ctab on their morphology *J Nanomater Mol Nanotechnol* 2:1–10
- Anis M, Shirsat M, Hussaini S, Joshi B, Muley G (2016) Effect of sodium metasilicate on structural, optical, dielectric and mechanical properties of ADP crystal *J Mater Sci Technol* 32: 62–67
- Antonuk L et al (2000) Strategies to improve the signal and noise performance of active matrix, flat-panel imagers for diagnostic x-ray applications. *Medical Physics* 27:289–306
- Arico AS, Bruce P, Scrosati B, Tarascon J-M, van Schalkwijk W (2005) Nanostructured materials for advanced energy conversion and storage devices. *Nat Mater* 4:366–377
- Baltog I, Baibarac M, Mihut L, Preda N, Velula T, Bucur C, Husanu M (2009) Vibrational properties of polyaniline functionalized PbI<sub>2</sub> Rom. *J Phys* 54:677–688
- Barnakov YA, Ito S, Dmitruk I, Tsunekawa S, Kasuya A (2001) Production and optical study of PbI<sub>2</sub> nanorod-like particles. *Scripta Materialia* 45:273–277
- Batra A, Carmichael-Owens C, Simmons M, Aggarwal M, Lal R (2005) Design of a solution crystal growth crystallizer with a versatile electronic reciprocal motion control for a crystals holder. *Crys Res Technol* 40:757–760
- Baxter JB, Aydil ES (2005) Nanowire-based dye-sensitized solar cells. *Appl Phys Letters* 86:053114
- Bennett PR et al (2003) Polycrystalline lead iodide films for digital X-ray sensors. *Nucl Ins Methods Phys Res A: Accel Spectrometers, Detect Assoc Equip* 505:269–272
- Bhavsar D, Saraf K (2003) Optical and structural properties of Zn-doped lead iodide thin films. *Mater Chem Phys* 78:630–636
- Burger C, Goerres G, Schoenes S, Buck A, Lonn A, von Schulthess G (2002) PET attenuation coefficients from CT images: experimental evaluation of the transformation of CT into PET 511-keV attenuation coefficients. *Eur J Nucl Med Mol Imaging* 29:922–927. <https://doi.org/10.1007/s00259-002-0796-3>
- Bushberg JT, Boone JM (2011) *The essential physics of medical imaging*. Lippincott Williams & Wilkins, Philadelphia
- Casady J, Johnson RW (1996) Status of silicon carbide (SiC) as a wide-bandgap semiconductor for high-temperature applications: a review. *Solid-State Electron* 39:1409–1422
- Chakrabarty N, Mukherjee A, Sinha S, Basu S, Meikap A (2014) Observation of correlated barrier hopping in blue luminescent PbI<sub>2</sub>. *Nanoparticles Phys E: Low-dimens Syst Nanostructures* 64:134–140
- Chen R, Wang R-J, Chen T, Shern C (2000) Studies on the dielectric properties and structural phase transition of K<sub>2</sub>SO<sub>4</sub> crystal. *J Phys Chem Solids* 61:519–527
- Cheng C et al (2009) Hierarchical assembly of ZnO nanostructures on SnO<sub>2</sub> backbone nanowires: low-temperature hydrothermal preparation and optical properties. *ACS Nano* 3:3069–3076
- Chow TP, Tyagi R (1994) Wide bandgap compound semiconductors for superior high-voltage unipolar power devices. *Electron Devices, IEEE Transactions on* 41:1481–1483
- Condeles J, Mulato M (2015a) Crystalline texture and mammography energy range detection studies of pyrolysed lead iodide films: effects of solution concentration. *Mater Chem Phys* 166:190–195
- Condeles JF, Mulato M (2015b) Crystalline texture and mammography energy range detection studies of pyrolysed lead iodide films: effects of solution concentration. *Mater Chem Phys* 166:190–195. <https://doi.org/10.1016/j.matchemphys.2015.09.048>
- Condeles J, Mulato M (2016) Polycrystalline lead iodide films produced by solution evaporation and tested in the mammography X-ray energy range. *J Phys Chem Solids* 89:39–44
- Condeles J, Lofrano R, Rosolen J, Mulato M (2006) Stoichiometry, surface and structural characterization of lead iodide thin films. *Brazilian J Phys* 36:320–323
- Condeles JF, Ghilardi Netto T, Mulato M (2007) Lead iodide films as X-ray sensors tested in the mammography energy region. *Nucl Inst Methods Phys Res A: Accel, Spectrometers Detect Assoc Equip* 577:724–728. <https://doi.org/10.1016/j.nima.2007.04.139>
- Dag I, Lifshitz E (1996) Dynamics of recombination processes in PbI<sub>2</sub> nanocrystals embedded in porous silica films. *J Phys Chem* 100:8962–8972. <https://doi.org/10.1021/jp952863y>
- Dmitriev Y, Bennett PR, Cirignano LJ, Klugerman M, Shah KS (2009) The electrical response of PbI<sub>2</sub> films to  $\gamma$ -ray irradiation and the limitation of film thickness. *Nucl Ins Methods Phys Res A: Accel Spectrometers Detect Assoc Equip* 599:192–195
- Dugan A, Henisch H (1967) Dielectric properties and index of refraction of lead iodide single crystals. *J Phys Chem Solids* 28:971–976
- El-Mallah H (2012) AC electrical conductivity and dielectric properties of perovskite (Pb, Ca) TiO<sub>3</sub> ceramic. *Acta Phys Polonica-A Gen Phys* 122:174
- El-Mallah H, Hegab N (2007) Studies on ac properties of Ca<sub>1-x</sub>Sr<sub>x</sub>TiO<sub>3</sub> perovskites. *J Mater Sci* 42:332–336
- Empedocles S et al. (2005) Methods of making, positioning and orienting nanostructures, nanostructure arrays and nanostructure devices. Google Patents No. 6,962,823
- Eperon GE, Paternò GM, Sutton RJ, Zampetti A, Haghighirad AA, Cacialli F, Snaith HJ (2015) Inorganic caesium lead iodide perovskite solar cells. *J Mater Chem A* 3:19688–19695
- Farhadi-Khouzani M, Fereshteh Z, Loghman-Estarki MR, Razavi RS (2012) Different morphologies of ZnO nanostructures via polymeric complex sol–gel method: synthesis and characterization. *J Sol-Gel Sci Technol* 64:193–199
- Feng M, Shen S-C, Caruth DC, Huang J-J (2004) Device technologies for RF front-end circuits in next-generation wireless communications. *Proc IEEE* 92:354–375
- Gafoor AA, Thomas J, Musthafa M, Pradyumnan P (2011) Effects of Sm<sup>3+</sup> doping on dielectric properties of anatase TiO<sub>2</sub> nanoparticles synthesized by a low-temperature hydrothermal method. *J Electron Mater* 40:2152
- Gafoor AA, Musthafa M, Pradyumnan P (2013) Effect of Nd<sup>3+</sup> doping on optical and dielectric properties of TiO<sub>2</sub> nanoparticles synthesized by a low temperature hydrothermal method. *J Nanosci nanotechnol* 1:53–57
- George MA, Azoulay M, Jayathirtha HN, Biao Y, Burger A, Collins WE, Silberman E (1994) Atomic force microscopy of lead

- iodide crystal surfaces. *J Cryst Growth* 137:299–303. [https://doi.org/10.1016/0022-0248\(94\)91289-0](https://doi.org/10.1016/0022-0248(94)91289-0)
- Ghosh T, Bandyopadhyay S, Roy K, Kar S, Lahiri A, Maiti A, Goswami K (2008) Optical and structural properties of lead iodide thin films prepared by vacuum evaporation method. *Cryst Res Technol* 43:959–963
- Glasser L, Hall P, Liebenberg D (1967) Dielectric properties of lead iodide. *Journal of the Chemical Society A: Inorganic, Physical, Theoretical* 0:295–296. <https://doi.org/10.1039/J19670000295>
- Goldberg M, Langer R, Jia X (2007) Nanostructured materials for applications in drug delivery and tissue engineering. *J Biomater Sci Polym ed* 18:241–268
- Hamdy MS, Saputera WH, Groenen EJ, Mul G (2014) A novel TiO<sub>2</sub> composite for photocatalytic wastewater treatment. *J Catal* 310:75–83
- Hassan MA, Jafar MM, Matuchova M, Bulos BN (2010) An experimental evidence of some lead iodide polytypes compatible with the dielectric functions model. *J Appl Sci* 10:3367–3373
- Henisch HK (1996) *Crystal growth in gels*. Dover Publications INC, New York
- Hill NE (1969) *Dielectric properties and molecular behaviour*. Van Nostrand Reinhold, New York
- Hubbell JH (1982) Photon mass attenuation and energy-absorption coefficients. *Int J Appl Radiat Isot* 33:1269–1290. [https://doi.org/10.1016/0020-708X\(82\)90248-4](https://doi.org/10.1016/0020-708X(82)90248-4)
- Kasi GK, Dollahon NR, Ahmadi TS (2007) Fabrication and characterization of solid PbI<sub>2</sub> nanocrystals. *J Phys D: Appl Phys* 40:1778
- Kaviyarasu K, Devarajan PA, SSSJ X, Thomas SA, Selvakumar S (2012a) One pot synthesis and characterization of cesium doped SnO<sub>2</sub> Nanocrystals via a hydrothermal process. *J Mater Sci Technol* 28:15–20
- Kaviyarasu K, Sajan D, Selvakumar MS, Augustine Thomas S, Prem Anand D (2012b) A facile hydrothermal route to synthesize novel PbI<sub>2</sub> nanorods. *J Phys Chem Solids* 73:1396–1400. <https://doi.org/10.1016/j.jpcs.2012.06.005>
- Khilji M, Sherman W, Wilkinson G (1982) Raman study of three polytypes of PbI<sub>2</sub> *Journal of Raman Spectroscopy* 13:127–133
- Kirschman RK (1999) *High temperature electronics*. IEEE Press, New York, NY
- Koops C (1951) On the dispersion of resistivity and dielectric constant of some semiconductors at audiofrequencies. *Phys Rev* 83:121
- Le Stanguennec M, Elliott S (1994) Frequency-dependent ionic conductivity in AgI-AgPO<sub>3</sub> glasses. *Solid State Ionics* 73:199–208
- Lee W, Liu JF, Nowick A (1991) Limiting behavior of ac conductivity in ionically conducting crystals and glasses: a new universality. *Phys Rev Letters* 67:1559
- Liang N et al (2014) AgIn<sub>x</sub>Ga<sub>1-x</sub>S<sub>2</sub> solid solution nanocrystals: synthesis, band gap tuning and photocatalytic activity. *Cryst EngComm* 16:10123–10130
- Lifshitz E, Yassen M, Bykov L, Dag I, Chaim R (1994) Nanometer-sized particles of lead iodide embedded in silica films. *J Phys Chem* 98:1459–1463
- Luo P, Xia W, Zhou S, Sun L, Cheng J, Xu C, Lu Y (2016) Solvent engineering for ambient-air-processed, phase-stable CsPbI<sub>3</sub> in perovskite solar cells. *The Journal of Physical Chemistry Letters* 7:3603–3608
- Ma D, Zhang W, Zhang R, Zhang M, Xi G, Qian Y (2005) A facile hydrothermal synthesis route to single-crystalline lead iodide nanobelts and nanobelt bundles. *J Nanosci Nanotechnol* 5:810–813
- Matuchova M, Zdansky K, Zavadil J, Maixner J, Alexiev D, Prochazkova D (2006) Study of lead iodide semiconductor crystals doped with silver. *Mater Sci Semicond Proc* 9:394–398
- Mirabbaszadeh K, Ahmadi M, Khosravi M, Mokhtari R, Salari S (2013) Hydrothermal synthesis of vertically aligned cesium-doped ZnO nanorods for solar cell applications. *J Inorg Organomet Polym Mater* 23:1219–1225
- Mohammadikish M, Davar F, Lohman-Estarki MR (2015) Various morphologies of nano/micro PbS via green hydrothermal method. *J Mater Sci: Mater Electron* 26:2937–2946
- Mousa AM, Jamil SS, Ponpon JP (2012) Effect of doping and post annealing on PbI<sub>2</sub> photoconductivity. *J Mater Sci Eng* 2:215–219
- Nambiar S, Yeow JT (2012) Polymer-composite materials for radiation protection. *ACS Appl Mater Interfaces* 4:5717–5726
- Nambiar S, Osei EK, JTW Y (2015) Bismuth sulfide nanoflowers for detection of X-rays in the mammographic energy range. *Sci Rep* 5:9440. <https://doi.org/10.1038/srep09440> <http://www.nature.com/articles/srep09440#supplementary-information>
- Novosad IS, Novosad SS (2013) Spectral characteristics of europium-doped lead iodide. *J Appl Spectros* 80:191–196. <https://doi.org/10.1007/s10812-013-9744-1>
- Park MH, Li JH, Kumar A, Li G, Yang Y (2009) Doping of the metal oxide nanostructure and its influence in organic electronics. *Adv Funct Mater* 19:1241–1246
- Pawar R et al (2010) Surfactant assisted low temperature synthesis of nanocrystalline ZnO and its gas sensing properties. *Sens Actuators B: Chem* 151:212–218
- Periyasamy BK, Jebas RS, Thailampillai B (2007) Synthesis and spectral studies of 2-aminopyridinium para-nitrobenzoate: a novel optoelectronic crystal. *Mater Letters* 61:1489–1491
- Ponpon J (2005) Semiconductor detectors for 2D X-ray imaging. *Nucl Inst Methods Phys Res A: Accel Spectrometers Detect Assoc Equip* 551:15–26
- Ponpon JP, Amann M (2004) Current instability and polarization phenomena in lead iodide crystalline detectors. *Nucl Inst Methods Phys Res A: Accel Spectrometers Detect Assoc Equip* 526:447–454. <https://doi.org/10.1016/j.nima.2004.03.136>
- Ragupathi V, Krishnaswamy S, Sada S, Nagarajan GS, Raman S (2014) Toward p-type conduction in Cs-doped ZnO: an eco-friendly synthesis method. *J Mater Sci* 49:7418–7424
- Rauf M, Meetani M, Hisaindee S (2011) An overview on the photocatalytic degradation of azo dyes in the presence of TiO<sub>2</sub> doped with selective transition metals. *Desalination* 276:13–27
- Retif P, Pinel S, Toussaint M, Frochot C, Chouikrat R, Bastogne T, Barberi-Heyob M (2015) Nanoparticles for radiation therapy enhancement: the key parameters. *Theranostics* 5:1030
- Roth S, Willig W (1971) Lead iodide nuclear particle detectors. *Appl Phys Letters* 18:328–330
- Sabourimanesh A, Rashidi A, Marjani K, Motamedara P, Valizadeh Y (2015) Effects of process parameters on the size of nanostructure magnesium oxide synthesized by a surfactant and ligand assisted wet chemical method crystal structure. *Theor Appl* 4:28

- Sandrock C, Kelty S, Hwang D (1986) Clusters in solution: growth and optical properties of layered semiconductors with hexagonal and honeycombed structures. *J Chem Phys* 85:5337–5340
- Scher E, Buretea MA, Chow C, Empedocles S, Meisel A, Parce JW (2005) Nanostructure and nanocomposite based compositions and photovoltaic devices, U.S. Patent No. 6,878,871. U.S. Patent and Trademark Office, Washington, DC
- Sears WM, Klein M, Morrison J (1979) Polytypism and the vibrational properties of Pb I 2. *Phys Rev B* 19:2305
- Sengupta A, Mandal K, Zhang J (2000) Ultrafast electronic relaxation dynamics in layered iodide semiconductors: a comparative study of colloidal BiI<sub>3</sub> and PbI<sub>2</sub> nanoparticles. *J Phys Chem B* 104:9396–9403
- Shakir M, Kushwaha S, Maurya K, Arora M, Bhagavannarayana G (2009a) Growth and characterization of glycine picrate—remarkable second-harmonic generation in centrosymmetric crystal. *J Cryst Growth* 311:3871–3875
- Shakir M, Kushwaha S, Maurya K, Bhagavannarayana G, Wahab M (2009b) Characterization of ZnSe nanoparticles synthesized by microwave heating process. *Solid State Commun* 149:2047–2049
- Shakir M, Singh B, Gaur R, Kumar B, Bhagavannarayana G, Wahab M (2009c) Dielectric behaviour and ac electrical conductivity analysis of ZnSe chalcogenide nanoparticles. *Chalcogenide Letters* 6:655–660
- Shakir M, Kushwaha S, Maurya K, Kumar S, Wahab M, Bhagavannarayana G (2010) Enhancement of second harmonic generation, optical and dielectric properties in L-asparagine monohydrate single crystals due to an improvement in crystalline perfection by annealing. *J Appl Crystallog* 43:491–497
- Shanmugam G, Thirupugalmani K, Rakhikrishna R, Philip J, Brahadeeswaran S (2013) Thermophysical, mechanical and dielectric studies on piperidinium p-hydroxybenzoate. *J Therm Anal Calorim* 114:1245–1254
- Shkir M, Aarya S, Singh R, Arora M, Bhagavannarayana G, Senguttuvan T (2012a) Synthesis of ZnTe nanoparticles by microwave irradiation technique, and their characterization. *Nanosci Nanotechnol Letters* 4:405–408
- Shkir M, Abbas H, Khan ZR (2012b) Effect of thickness on the structural, optical and electrical properties of thermally evaporated PbI<sub>2</sub> thin films. *J Phys Chem Solids* 73:1309–1313
- Shkir M et al (2014) Optical spectroscopy, crystalline perfection, etching and mechanical studies on P-nitroaniline (PNA) single crystals. *Opt Mater* 36:675–681
- Shkir M, Yahia IS, AlFaify S, Abutalib MM, Muhammad S (2016a) Facile synthesis of lead iodide nanostructures by microwave irradiation technique and their structural, morphological, photoluminescence and dielectric studies. *J Mol Struct*, 1110:83–90. <https://doi.org/10.1016/j.molstruc.2016.01.014>
- Shkir M, Yahia IS, Ganesh V, Algarni H, AlFaify S (2016b) Facile hydrothermal-assisted synthesis of Gd<sup>3+</sup> doped PbI<sub>2</sub> nanostructures and their characterization. *Mater Letters* 176:135–138. <https://doi.org/10.1016/J.Matlet.2016.04.062>
- Shkir M, AlFaify S, Yahia IS, Ganesh V, Shoukry H (2017) Microwave-assisted synthesis of Gd<sup>3+</sup> doped PbI<sub>2</sub>. Hierarchical Nanostruct Optoelectron Radiat Detect Appl Phys B: Condens Matter 508:41–46. <https://doi.org/10.1016/J.Physb.2016.12.016>
- Srivastava P, Singh K (2014) Effects of Cs-doping on morphological, optical and electrical properties of Bi<sub>2</sub>Te<sub>3</sub> nanostructures. *Mater Lett* 136:337–340
- Street RA et al. (1999) X-ray imaging using lead iodide as a semiconductor detector. In: *Medical Imaging'99*. International Society for Optics and Photonics, pp 36–47. <https://dx.doi.org/10.1117/12.349504>
- Street R et al (2002) Comparison of PbI<sub>2</sub> and HgI<sub>2</sub> for direct detection active matrix x-ray image sensors. *J Appl Phys* 91:3345–3355
- Tang ZK, Nozue Y, Goto T (1995) Raman scattering in PbI<sub>2</sub> clusters incorporated into zeolite cages. *Mater Sci Eng: B* 35:410–416. [https://doi.org/10.1016/0921-5107\(95\)01394-6](https://doi.org/10.1016/0921-5107(95)01394-6)
- Tonn J, Danilewsky AN, Cröll A, Matuchova M, Maixner J (2011) Czochralski growth of lead iodide single crystals: investigations and comparison with the Bridgman method. *J Cryst Growth* 318:558–562. <https://doi.org/10.1016/j.jcrysgro.2010.10.059>
- Tonn J, Matuchova M, Danilewsky AN, Cröll A (2015) Removal of oxidic impurities for the growth of high purity lead iodide single crystals. *J Cryst Growth* 416:82–89. <https://doi.org/10.1016/j.jcrysgro.2015.01.024>
- Tubbs M, Forty A (1964) Photographic applications of lead iodide. *Br J Appl Phys* 15:1553
- Vavilov VS (1994) Physics and applications of wide bandgap semiconductors *Physics-Uspeski* 37:269–277
- Vogel R, Hoyer P, Weller H (1994) Quantum-sized PbS, CdS, Ag<sub>2</sub>S, Sb<sub>2</sub>S<sub>3</sub>, and Bi<sub>2</sub>S<sub>3</sub> particles as sensitizers for various nanoporous wide-bandgap semiconductors the journal of physical chemistry 98:3183–3188
- Warren R, Liang W (1993) Raman spectroscopy of new lead iodide intercalation compounds. *J Phys: Condens Matter* 5:6407
- Wilke K, Breuer H (1999) The influence of transition metal doping on the physical and photocatalytic properties of titania. *J Photochem Photobiol A: Chem* 121:49–53
- Xu M, Zai J, Yuan Y, Qian X (2012) Band gap-tunable (CuIn)<sub>x</sub>Zn<sub>2</sub>(1-x)S<sub>2</sub> solid solutions: preparation and efficient photocatalytic hydrogen production from water under visible light without noble metals. *J Mater Chem* 22:23929–23934
- Xue D, Kitamura K (2002) Dielectric characterization of the defect concentration in lithium niobate single crystals. *Solid state Commun* 122:537–541
- Yu Y et al (2015) Development of lead iodide perovskite solar cells using three-dimensional titanium dioxide nanowire architectures. *ACS Nano* 9:564–572
- Zentai G, Schieber M, Partain L, Pavlyuchkova R, Proano C (2005) Large area mercuric iodide and lead iodide X-ray detectors for medical and non-destructive industrial imaging. *J Cryst Growth* 275:e1327–e1331. <https://doi.org/10.1016/j.jcrysgro.2004.11.105>
- Zhang J, Song T, Zhang Z, Ding K, Huang F, Sun B (2015) Layered ultrathin PbI<sub>2</sub> single crystals for high sensitivity flexible photodetectors. *J Mater Chem C* 3:4402–4406. <https://doi.org/10.1039/c4tc02712d>
- Zhao G, Wu Y, Shao Y, Hao X (2016) Large-quantity and continuous preparation of two-dimensional nanosheets. *Nanoscale* 8(10):5407–5411
- Zhu X, Wei Z, Jin Y, Xiang A (2007) Growth and characterization of a PbI<sub>2</sub> single crystal used for gamma ray. *Detect Cryst Res Technol* 42:456–459



Zhu G, Liu P, Hojamberdiev M, Zhou J-P, Huang X, Feng B, Yang R (2010) Controllable synthesis of PbI<sub>2</sub> nanocrystals via a surfactant-assisted hydrothermal route. *Appl Phys A* 98:299–304

Zhu X, Sun H, Yang D, Zheng X (2012) Growth, surface treatment and characterization of polycrystalline lead iodide thick films prepared using close space deposition technique, 10. *Nucl Inst Methods Phys Res A: Accel spectrometers Detect Assoc Equip* 691:–15. <https://doi.org/10.1016/J.Nima.2012.07.003>